THE PORE STRUCTURE OF COMPACTED AND PARTLY SATURATED MX-80 BENTONITE AT DIFFERENT DRY DENSITIES

Lukas M. Keller[1],*, Ali Seiphoori[2], Philippe Gasser[3], Falk Lucas[3], Lorenz Holzer[1], and Alessio Ferrari[2]

[1] Zürich University of Applied Sciences, Winterthur, Switzerland
[2] Ecole Polytechnique Fédérale de Lausanne (EPFL), School of Architecture, Civil and Environmental Engineering (ENAC), Laboratory for Soil Mechanics (LMS), Switzerland
[3] Swiss Federal Institute of Technology, Centre for Imaging Science and Technology, Zürich, Switzerland

Abstract—Compacted MX-80 bentonite is a potential backfill material in radioactive-waste repositories. Pore space in MX-80 has been the subject of considerable debate. 3D reconstructions of the pore space based on tomographic methods could provide new insights into the nature of the pore space of compacted bentonites. To date, few such reconstructions have been done because of problems with the preparation of bentonite samples for electron microscopy. The nanoscale intergranular pore space was investigated here by cryo-Focused Ion Beam nanotomography (FIB-nt) applied to previously high-pressure frozen MX-80 bentonite samples. This approach allowed a tomographic investigation of the *in situ* microstructure related to different dry densities (1.24, 1.46, and 1.67 g/cm^3). The FIB-nt technique is able to resolve intergranular pores with radii >10 nm. With increasing dry density (1.24−1.67 g/cm^3) the intergranular porosity (>10 nm) decreased from ~5 vol.% to 0.1 vol.%. At dry densities of 1.24 and 1.46 g/cm^3, intergranular pores were filled with clay aggregates, which formed a mesh-like structure, similar to the honeycomb structure observed in diagenetic smectite. Unlike 'typical' clay gels, the cores of the honeycomb structure were not filled with pure water, but instead were filled with a less dense material which presumably consists of very fine clay similar to a colloid. In the low-density sample this honeycomb-structured material partly filled the intergranular pore space but some open pores were also present. In the 1.46 g/cm^3 sample, the material filled the intergranular pores almost completely. At the highest densities investigated (1.67 g/cm^3), the honeycomb-structured material was not present, probably because of the lack of intergranular pores which suppressed the formation of the honeycomb framework or skeleton consisting of clay aggregates.

Key Words—Clay Gels, Cryo-sample Preparation, MX-80 Bentonite, Nanotomography.

INTRODUCTION

The engineering concepts for radioactive-waste repositories include a barrier system which consists of a sealing material that surrounds the waste canisters and fills (*i.e.* backfill) the cavities between the canisters and the borehole in the host rock. Bentonite is considered a potential backfill material (*e.g.* Bucher and Müller-Vonmoos, 1989; Gens, 2010). An advantage of bentonite is its large swelling capacity; under confined conditions, the compaction results in consolidation into a dense material. A final assessment of its suitability as a backfill material requires an understanding of the microstructure response to compaction. In particular, understanding reduction of porosity and pore connectivity due to compaction and associated increase in density is critical when evaluating the sealing property of the material (*e.g.* Saiyouri *et al.*, 2000; Delage and Cui, 2007; Monroy *et al.*, 2010). To date, insight into the chemical and physical properties of bentonite has been

achieved by analytical and experimental work (*e.g.* Herbert *et al.*, 2004; Lloret and Villar, 2007). Detailed knowledge of the microstructural properties corresponding to variable bulk physical properties is still lacking. In the context of its application as a backfill material and corresponding sealing behavior, microstructural investigations of the nanoscale pore space in bentonites using high-resolution imaging techniques are scarce, the work of Pusch (2001) and Holzer *et al.* (2010) being exceptions. At larger length scales, other studies used X-ray computed microtomography to study the microstructure of bentonites (*e.g.* Tomioka *et al.*, 2010).

Bentonite is also employed in other engineering applications such as drilling fluids where it is used in the form of suspensions where the flow behavior is of major concern (*e.g.* Luckham and Rossi, 1999). Bentonite suspensions have much lower concentrations of clay (solid loading) in comparison to bentonite used as a sealing material. Regardless of the clay concentration, the main challenge to the study of bentonite microstructures is sample preparation. For electron-beam imaging the samples must be stable under high vacuum. Drying may induce significant artifacts associated with shrinking, however. In addition, the softness of the material also posed a challenge as bentonite and its

microstructure are prone to undesirable mechanical modifications that can occur during sample preparation. Hence, for quantitative microscopic investigations of compacted and hydrated bentonite, the development of methods that enable the stabilization and preservation of the original pore structure is crucial. To overcome these problems, several methods have been applied to prepare bentonite samples for electron-beam imaging. The methodological developments in bentonite-sample preparation over the last five decades along with the difficulties encountered were summarized by Bhuiyan (2013). Regarding bentonite suspensions, the rearrangement of clay particles during sample preparation was of major concern. Cryofixation techniques in combination with cryo-SEM/TEM prevented rearrangement of particles and over the years these methods began to offer promise in terms of the investigation of the microstructures of bentonite suspensions (Vali and Hesse, 1992; Gu and Doner, 1993; Bhuiyan, 2013). The most critical aspect of these cryofixation techniques was the cooling rate. If the cooling rate is too slow, the formation of ice crystals and phase separation can affect the original bentonite microstructure (Vali and Hesse, 1992). To achieve the necessary cooling rates that allow vitrification of the pore water, the sample thickness must be minimized. The present study used a state-of-the-art, high-pressure freezing instrument that was able to freeze samples with a thickness of 200 μm within milliseconds so that they were completely vitrified. This method was first used by Velbel and Barker (2008) and Holzer *et al.* (2010), among others, who applied this method in combination with cryo-SEM in the investigation of wet geological clayey samples. For conventional high-pressure freezing, the samples must be transferred into small sample holders. The degree of compaction could not be controlled during the transfer into the sample holder.

For the present study a new procedure for high-pressure freezing of compacted bentonite samples was developed. In order to study pore-space evolution as function of dry density, re-hydrated bentonite samples with well defined properties (*e.g.* dry densities, water content, total porosity) were produced directly in the sample holders of the high-pressure freezing instrument. This approach required the fabrication of light bentonite samples, so that the volume of compacted material was equivalent to the volume of the small sample holders. This procedure required an exceptionally precise balance. After weighing the correct amount of material to match the target density, the bentonite material was placed directly into the sample holder of the high-pressure freezing system and compacted there. Then the samples were analyzed in a frozen state using cryo-FIB-nt. This approach avoided the artifacts which emerge if the samples are dried prior to microscopic investigation. In addition, the approach also avoided effects arising from mechanical preparation, ice-crystal formation, and

phase separation due to conventional freezing. Thus, everything that is technically feasible was done to preserve the original microstructure from partially hydrated bentonite samples with different bulk densities.

A major constituent of bentonites is montmorillonite, which is a member of the smectite family. Diffusive solute transport in such a system is complicated by the fact that mineral layer surfaces are negatively charged, which is compensated by exchangeable cations located between the mineral layers. Diffusion models often assume that transport of chemical species occurs along two different types of pathways, one of which is the charged surfaces of mineral layers (*i.e.* interlayer region), while the other corresponds to larger water-filled pores where transport occurs largely unaffected by surface charging (*e.g.* Appelo, 2013). The actual contribution of the two pathways to solute transport is subject to discussion (*e.g.* Glaus *et al.*, 2013). Experimental data on cation diffusion were explained by simultaneous transport along the two different pathways (*e.g.* Bourg *et al.*, 2007). In contrast, tracer diffusion experiments suggested that surface diffusion dominates cation diffusion (Glaus *et al.*, 2007). Anion diffusion is often modeled using the assumption that these species are strongly repelled from the clay-mineral surfaces and thus the predominant diffusion path for anionic species are larger, water-filled pores (Pusch *et al.*, 1990). On the basis of experimental diffusion data, this assumption allowed the determination of diffusion-accessible porosity, which was interpreted as the water-filled porosity or intergranular porosity. The calculated diffusion-accessible porosities are inconsistent, however, and depend on the diffusion models used (Tournassat and Appelo, 2011), which led to the suggestion that porosities calculated from diffusion data lack physical meaning. FIB-nt is able to resolve intergranular pores with radii >~10 nm, but is unable to resolve the nanopores between mineral layers of smectite minerals. From a microstructural point of view, the approach used was a first attempt to shed light on the nature of the pore space in dense compacted bentonites. The microstructural data acquired correspond to well defined bentonite samples and conclusions were reached on the nature of the disputed diffusion pathways (*i.e.* intergranular pores).

SAMPLE PREPARATION

MX-80 bentonite was first sieved to a grain size of <90 μm (powder form) in order to achieve maximum homogeneity. In order to saturate the dry material, the powder was vapor-phase hydrated. The powder was placed in a humid chamber that was set to 100% relative humidity. After ~4−5 weeks the bentonite powder reached the target water content. Liquid-water saturation was found to be unsuitable due to aggregation of the powder which resulted in inhomogeneous distribution of

Table 1. Properties of the samples prepared for the FIB analysis.

| Sample name | Holder | | Compacted powder | | Target values | | | Mass of compacted wet soil + holders (g) | Mass of compacted wet soil (g) | Final sample properties | | | |
	Weight of top cap (g)	Weight of bottom cap (g)	Water content, w^* (-)	Ψ^{**} (MPa)	ρ_d, target (g/cm³)	Target dry mass (g)	Target wet mass (g)			ρ_d (g/cm³) (dry)	ρ_{bulk} (g/cm³) (wet)	Porosity, n(-)	Degree of saturation, S_r(-)
7,W.1.3	0.0226	0.0264	0.313	3.85	1.3	0.0051	0.0067	0.0553	0.0063	1.23	1.62	0.55	0.70
3,W.1.5	0.0226	0.0258	0.226	13.86	1.5	0.0059	0.0072	0.0554	0.0070	1.46	1.80	0.46	0.71
4,W.1.7	0.0225	0.0254	0.226	13.86	1.7	0.0067	0.0082	0.0559	0.0080	1.67	2.05	0.39	0.97

* Target water content was achieved by hydration in the vapor phase.
** Values measured by a dewpoint potentiometer system (WP4C device, Decagon, 2002).

the water within the bentonite samples. Homogenization of water was better achieved in the vapor form. Water contents of 22.6 wt.% and 31.3 wt.% were obtained in this way, corresponding to 13.86 and 3.85 MPa of total suctions, respectively (Table 1). Total suction was measured using a dewpoint potentiometer system (WP4C device; Decagon, 2002).

By considering the water content of the hydrated powder and the volume of the sample holder, a calculated amount of the hydrated material was balanced and compacted between two holders of the high-pressure freezing apparatus to make a sample with a target thickness of 200 μm and a diameter of 5 mm. This cylindrical dimension resulted in a target volume of 3.9270 mm³. The target dry bulk densities of 1.3, 1.5, and 1.7 g/cm³ and high degrees of saturation were considered for the final state of the compacted material. The sample properties in terms of degree of saturation and porosity after preparation and back analyses are listed in Table 1. Compaction of the material was achieved using a special compaction mold within the sample holder of the high-pressure freezing apparatus. Then the sample holders were sealed in small clamps and, in order to preserve the water contents of the samples, the clamps were sealed using paraffin films.

Electron microscopy (FIB/scanning electron microscopy – SEM/transmission electron microscopy – TEM) requires drying of the samples prior to analysis. In order to prevent artifacts, the following procedure was applied (Figure 1). After compaction, the two aluminum half shells including the bentonite slabs were frozen under high pressure (2100 bar) and within milliseconds using the HPM 100 (Leica) high-pressure freezing system. Freezing at high pressure occurs by the injection of pressurized liquid nitrogen. This treatment prevented the formation of ice crystals which otherwise would have affected the delicate framework of the pore space. Using a freeze-fracture system (BAF 060, Baltec), the samples were coated with metal in the frozen state in order to prevent surface charging during FIB-nt. A cryo-transfer device was then used to transport the frozen material to a FIB/SEM instrument (Helios Nanolab 600i from FEI) equipped with an integrated cryo-stage. In this instrument, Focused Ion Beam nanotomography (FIB-nt) was applied to the material in the frozen state.

ANALYTICAL METHODS

Cryo-Focused Ion Beam nanotomography (FIB-nt)

Cryo-Focused Ion Beam nanotomography is done with dual-beam FIB-SEM instruments in which the ion and electron beams intersect under an angle of 52° at a focal point on the sample surface. In order to analyze frozen samples, the instrument is equipped with a cryo-stage, which allows a cooling of the sample down to −125ºC. Before FIB-nt the samples were coated with metal in the freeze-fracturing instrument. The transfer of
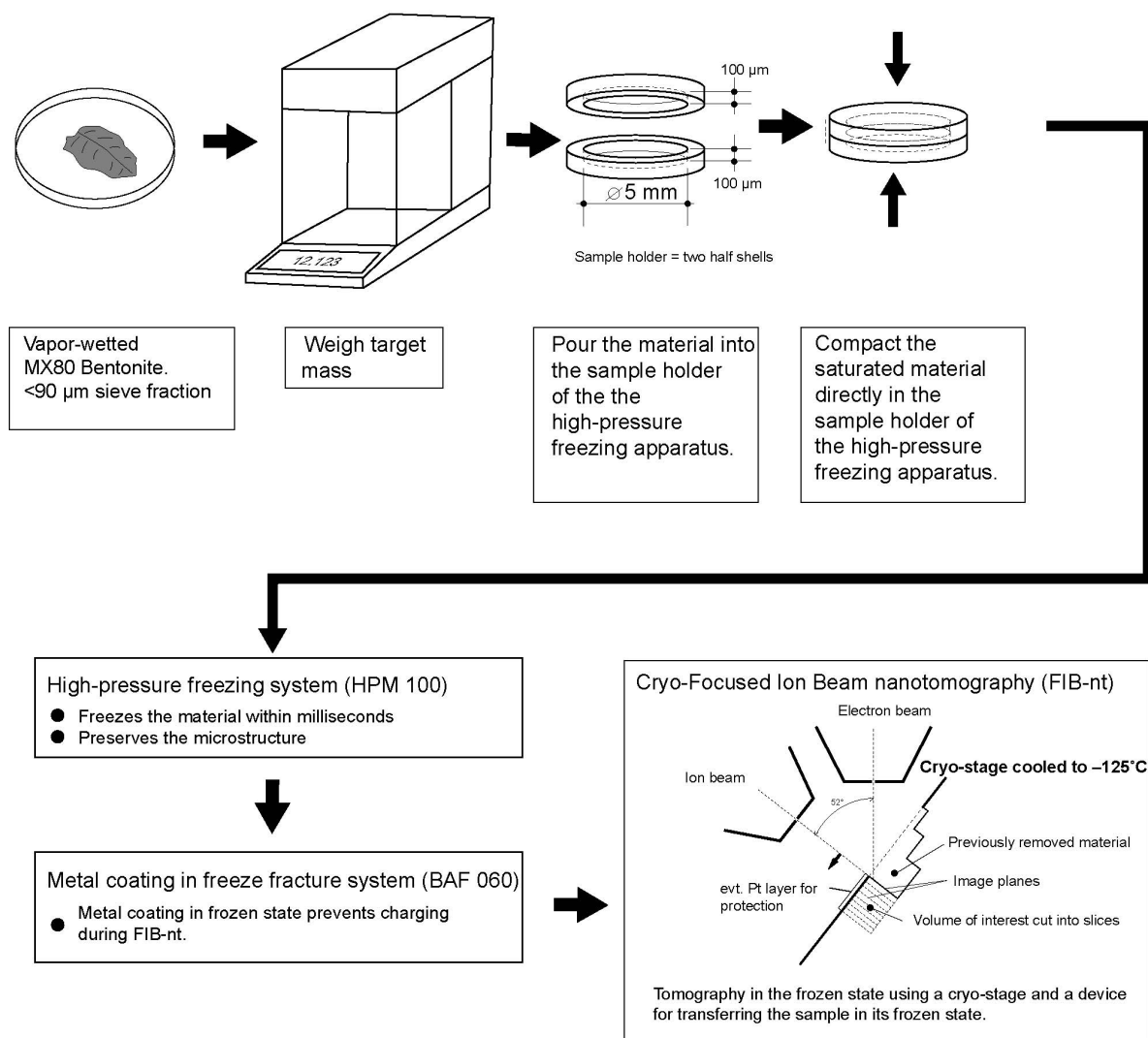
Figure 1. Overview of the methodological approach applied. A calculated amount of vapour-wetted bentonite is compacted in the sample holder of the high-pressure freezing instrument to the required density (see Table 1 and text). The sample is then frozen and analyzed by Focused Ion Beam nanotomography (FIB-nt).

the frozen samples between different instruments (freeze-fracturing instrument to the FIB-SEM) was achieved using a vacuum cryo-transfer system. The 3D information was obtained by acquiring a sequence of cross-sectional images by alternating FIB-slicing and SEM-imaging. The acquired series of images was spaced evenly through a region of the bulk specimen. A stack of these two-dimensional images was then transformed into a three-dimensional representation of the microstructure in the sample. The serial sectioning process began by the milling of a wedge-shaped trench in the sample. The current for ion milling was set at 700 pA. The 'front wall' of the trench was chosen as the initial cross section, which was imaged by the electron beam. After imaging, the ion beam was used to remove a layer of uniform thickness from the front wall, and thus the

cross-sectional plane advanced over a predetermined distance through the sample volume. The next electron image was collected from the fresh cross-section. By repeating this alternating milling/imaging process, the cross section advanced through the targeted volume, which resulted in a stack of 2D images.

For the present study, a FEI Helios Nanolab 600i FIB/ SEM instrument was used and important instrument setup parameters are listed below. A problem with Cryo-FIB-nt is image-surface charging; this affects the image quality. In order to suppress the effects of surface charging, BSE image stacks only were collected. Backscattered electrons have higher energies when compared to secondary electrons and are therefore less deflected by charged surfaces. For BSE imaging and to prevent charging effects, a low-acceleration voltage of

Table 2. Properties of FIB-nt data sets.

Sample	Volume of image stack (μm)	Porosity (vol.%)	Smallest pore radii (nm)	Figures
7,W.1.3	$17.1 \times 11.2 \times 5.8$	5.6	10	2a, 3, 5, 6
3,W.1.5	$14.7 \times 8.5 \times 1.7$	(no quantification, low quality)	–	7, 8, 9
4,W.1.7	$7.6 \times 12.0 \times 3.0$	0.1	10	2b, 10

1.0 kV and a beam current of 0.34 nA was used. An advantage of BSE images is the notable image contrast between pores and surrounding material which facilitates the image segmentation. The absolute size of the volumes analyzed, resolved pore radii and bulk porosity are listed in Table 2. The quality of the image stack of the sample with a density of ~1.5 g/cm^3 was poor and only allowed a segmentation of the gel-like material. The poor image quality was related to the unloading problems of electric charges from the thermally isolated cryo-stage during acquisition of the image stack. This problem did not appear during the acquisition of the other two image stacks. For the 1.5 g/cm^3 sample, single high-quality 2D BSE images of FIB-prepared cross-sections were acquired.

Image analysis

The position of single BSE images was aligned (in *x* and *y* coordinates) relative to the next successive image in the sequence (*z* direction) using a difference-minimization algorithm that is implemented in the freely available image-processing software, *Fiji* (http://fiji.sc/Fiji). The maximum overlapping area of an orthogonal cube was cropped from the aligned BSE image stack. Noise in the BSE images was reduced by application of an edge-preserving 3D median filter available in the *Avizo* software (http://www.vsg3d.com/avizo/overview). The reconstruction of a 3D microstructure required the segmentation of solid and pore phases in the images, *i.e.* the voxels representing either particles or pores have to be identified in the images and labeled accordingly. In addition, attempts were made to segment the honeycomb structure (see below) of the 'gel-like' material. Segmentation was done by means of tools for pore segmentation provided in the *Avizo* software. The procedure starts with a so-called range calibration of the image stack, which involves the calculation of a gray-level histogram showing number of voxels *vs.* gray values. In this histogram the peak, which corresponds to pore voxels, was identified and the range of gray values corresponding to pore voxels was determined by the position of the minima separating the pore-voxel peak from peaks of other phases. The application of an edge-preserving 3D media filter to the image stack reduced the noise. The pore voxels were then segmented from the images by intensity thresholding, which is applied according to the preset range calibration and can be adjusted interactively based on visual inspection. The information from segmentation was then combined into a single 3D volume. For 3D visualization, the *Avizo* software was used.

RESULTS

The porosity resolved and comparison based on qualitative observations

Here, the focus was on the intergranular porosity (*i.e.* radii >10 nm) that could be resolved by FIB-nt. Porosity was determined on the basis of the segmented image stacks and corresponds to the ratio between void volume and the analyzed volume.

All microstructures contained open and air-filled pores but to very different extents (Figure 2). At dry densities of ~1.7 g/cm^3 only very few isolated pore objects were observed (Figure 2b). The appearance was dense and the material lacked a clay gel. At lower densities (1.24 and 1.46 g/cm^3) the material contained clay aggregates, which formed a mesh-like framework or skeleton similar to the honeycomb structure observed in diagenetic smectites (*e.g.* Tompkins, 1981). This mesh-like material was found to be structurally distinct from clay gels which form from clay suspensions (see below). A greater fraction of pores was only observed at the lowest dry densities (1.24 g/cm^3) (Figure 2a).

FIB/SEM analysis: dry density ≈ 1.2 g/cm^3

A 3D reconstruction of the pore space in bentonite with a dry density of 1.2 g/cm^3 is shown in Figure 3 which is based on the BSE-stack from FIB-nt. At this density, bentonite contained a significant number of intergranular pores with radii >10 nm which formed due to geometric incompatibilities between clay grains with a grain size of a few microns (Figure 3). The image volume analyzed contained a relatively large non-clayey mineral grain, which occupied a large portion of the volume. Note that pores were mainly found in the fine-grained clay matrix. Hence, the segmented pore volume was related to the volume of the fine-grained matrix, which yielded a porosity of ~5.5 vol.% of the clay matrix. Continuous pore-size distributions (Münch and Holzer, 2008) were then determined for the observed intergranular porosity. The cumulative size distributions are shown in Figure 4a. The dashed curve represents the pore-size distribution of bentonite with a dry density of 1.2 g/cm^3. The corre-
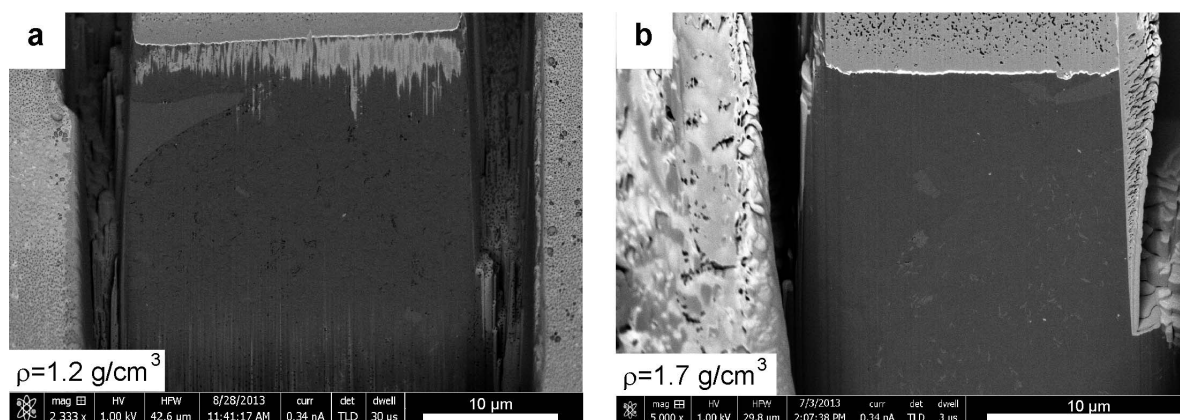
Figure 2. (a,b) BSE images showing the material analyzed by cryo FIB-nt. Note the difference in intergranular porosity between the two samples. The resolved pores are filled with air indicating that the water is mainly stored in the interlayer region.

sponding pore radii ranged between 10 and 250 nm with the majority of pores having radii of ~50 nm. The resolved pore space consisted of large numbers of predominantly unconnected pore objects. In Figure 3b each pore object was labeled with a different color. Based on visual inspection, greater connectivity was observed in the vicinity of the large non-clayey grain (Figure 3). One might argue that this is an artifact related to sample preparation. Close inspection, however, showed that these pores are bridged by delicate clay aggregates (Figure 3c). In the case of an artifact, these bridges should have broken, which was not the case. Larger pores around the non-clayey grain were considered as an original micro-structural property of the material at the given bulk properties (*i.e.* lower densities).

At the density under consideration, bentonite contained porous domains which consisted of a mesh-like framework of clay aggregates, which are arranged in a manner similar to the honeycomb structure observed in diagenetic smectites (Figures 5, 6). The cells in this honeycomb framework are partly filled with a colloidal material (Figure 5c). To a certain extent, this material resembled a clay gel, which was also observed in clay suspensions (see below and Luckham and Rossi, 1999 for a review). For the cell cores in the framework, a volume fraction of ~26 vol.% was determined (Figure 6c). The thickness of the clay aggregates making up the framework ranged between ~20 and 50 nm (Figure 5), suggesting that the walls consisted of several parallel clay platelets. Pore radii related to this clay skeleton were in the 10−100 nm range (Figure 6c and dotted curve in Figure 4b). In addition, a 3D reconstruction of the mesh-like framework revealed an anisotropic structure (Figure 6c).
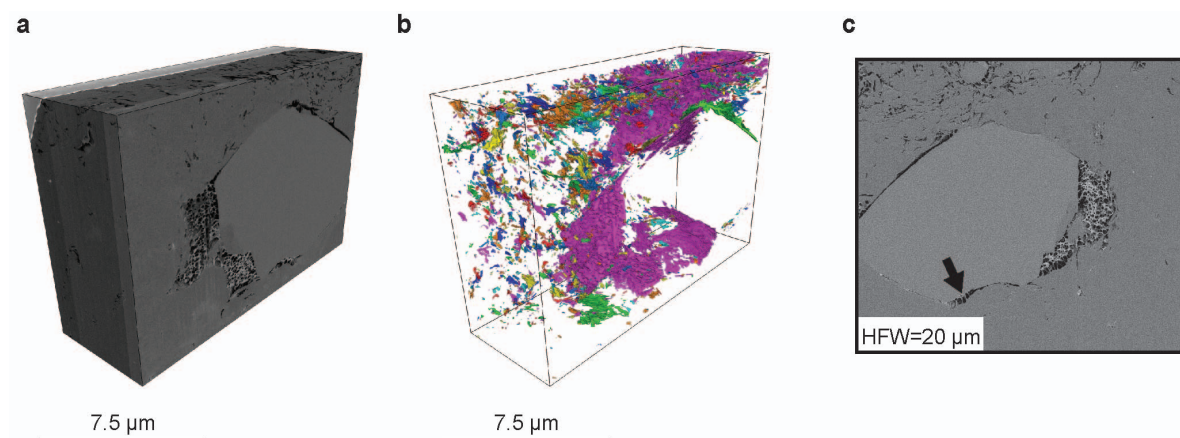

Figure 3. Visualization of FIB-nt data from bentonite using a density of 1.2 g/cm^3. (a) Reconstruction of the volume of material analyzed based on BSE images. Note, the large non-clayey mineral grain and the mesh-like framework or skeleton along its boundary (see discussion). (b) 3D reconstruction of the pore space. The colors indicate individual pore objects. (c) BSE image showing that pores between the non-clayey grain and the clay matrix are bridged by filigree clay aggregates (black arrow). This indicates that the larger intergranular pores are not an artifact from sample preparation but a genuine part of the microstructure.
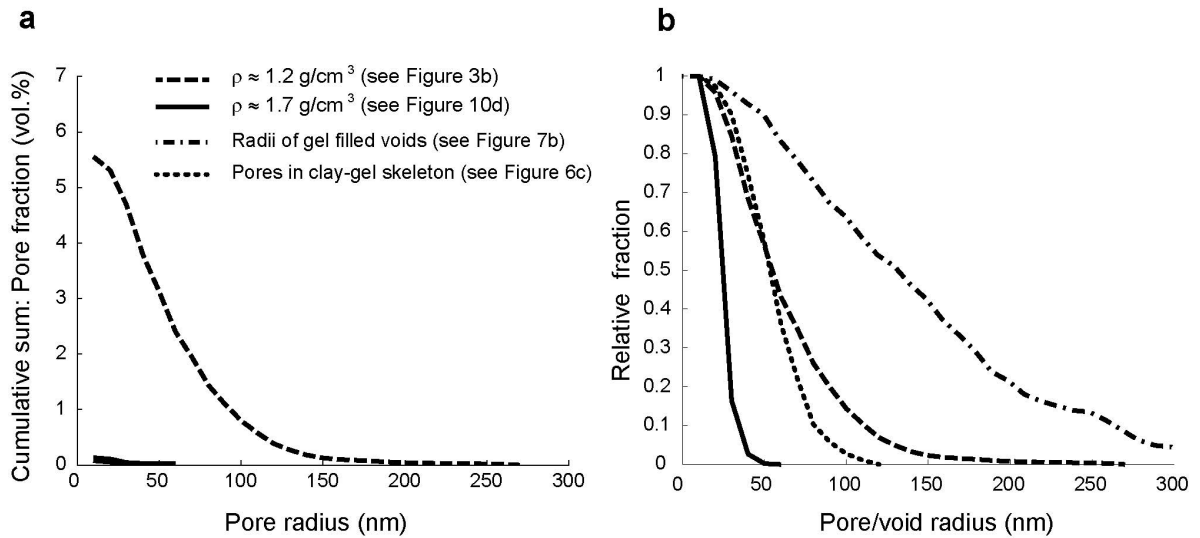
Figure 4. (a) Continuous pore-size distributions relative to dry bulk densities of 1.2 and 1.7 g/cm^3 obtained by analysis of image stacks from FIB-nt. (b) Plot shows the relative distributions of pore/void sizes (*i.e.* total pore volume normalized to 1), which allows comparison between different materials or different domains within one material. The dashed line corresponds to the pore space depicted in Figure 3b (bentonite with density 1.2 g/cm^3). The solid line corresponds to the pore space depicted in Figure 10b (1.7 g/cm^3). The dotted/dashed line corresponds to the gel-filled voids = Figure 7b (1.5 g/cm^3). The dotted line corresponds to an open pore of the clay-gel skeleton (Figure 6c).
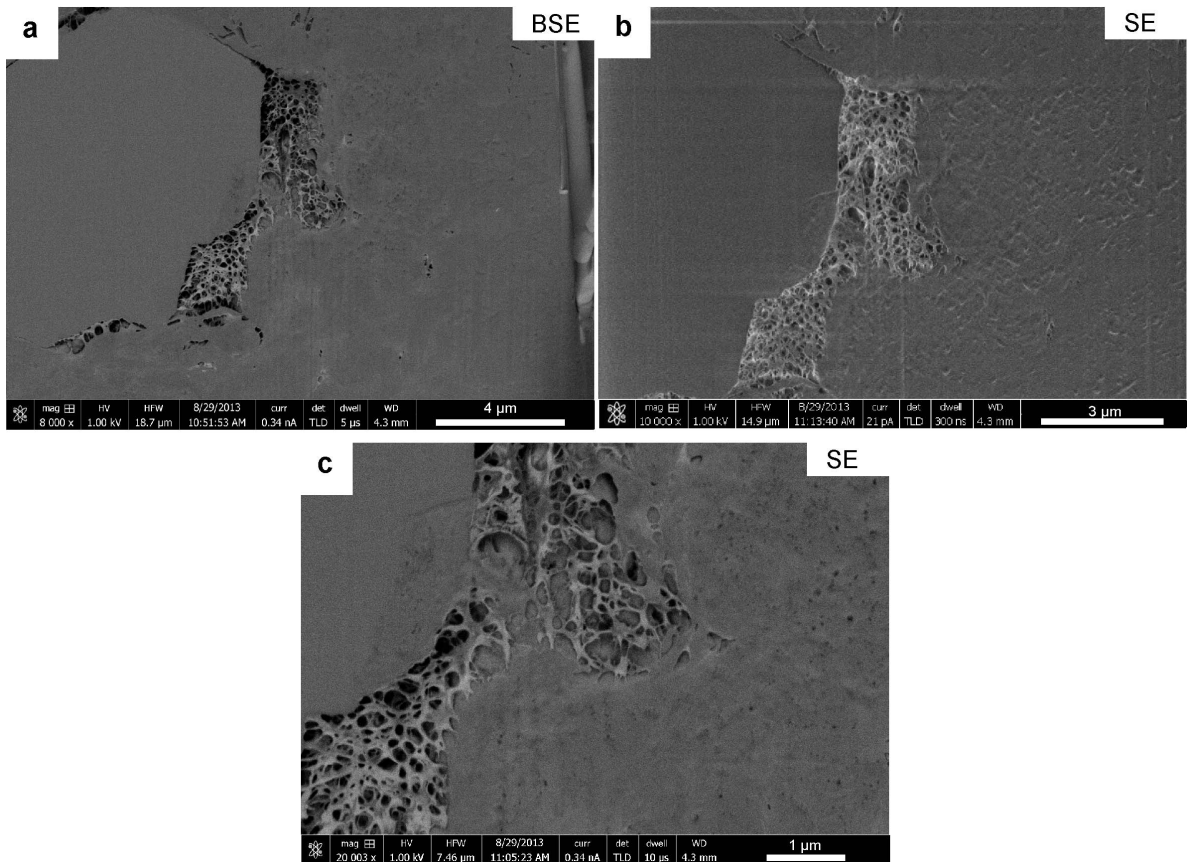

Figure 5. BSE and SE images of bentonite with a density of 1.2 g/cm^3, showing the mesh-like framework. (a) Overview showing that the framework is formed along the boundary of non-clayey grains. (b) SE image of the framework. (c) BSE image at higher magnification reveals that the network is partly filled with some other material (*i.e.* a colloidal gel).
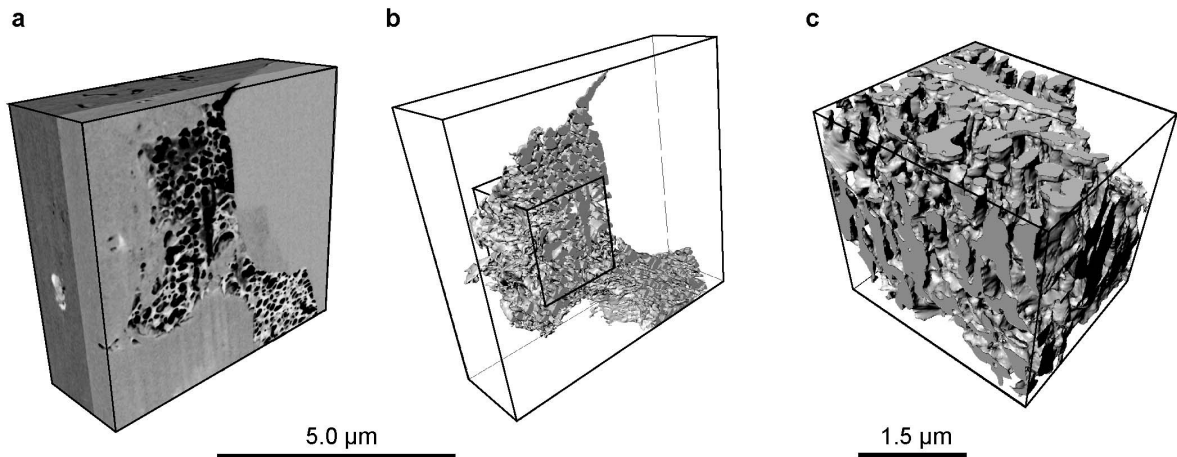
Figure 6. 3D visualizations of the mesh-like framework of the clay gel (in bentonite with a density of 1.2 g/cm^3). (a) 3D reconstruction of the material analyzed based on BSE images (the sub-volume was cropped from the volume of material depicted in Figure 3a). (b) 3D reconstruction of the open pore space in framework. The black cube indicates the sub-volume shown in Figure 6c. (c) Detail showing the geometry of the open pore space in the mesh-like framework. The image shows that the pore space is anisotropic.

FIB/SEM analysis: density ≈ 1.5 g/cm^3

Problems related to surface charging affected the image quality significantly but a segmentation of the image stack into a clay matrix and a honeycomb structural material was possible with reasonable accuracy (Figures 7, 8, 9). A 3D reconstruction of the void space filled with a honeycomb-structured material is given in Figure 7b. The clay gel fills the voids between clay grains. The radii of these filled voids ranged between 10 and 300 nm (Figure 4b, dashed/dotted curve). Based on high-quality BSE images, which were acquired after FIB-nt, no open pores were detected in the bentonite sample (Figure 8).

After imaging in the frozen state, the sample was heated slowly under high vacuum in order to sublimate the free water (*i.e.* amorphous ice) that presumably fills the pores. Under the high vacuum of ~10^{-4} Pa, sublimation began at temperatures of ~-110ºC. BSE images at -125ºC, -90ºC, and a SE image at room temperature are shown in Figure 9. Note that the cores of the honeycomb structure were still filled with some low-

density material even at room temperature, very unlike the behavior in sublimation experiments performed with frozen bentonite suspensions (*e.g.* Bhuiyan, 2013). In the latter case the clay aggregates were embedded in vitrified water (*e.g.* Bhuiyan, 2013) and sublimation allowed etching of ice in order to reveal the structure. In contrast, the filling of the honeycomb structure in the investigated bentonite could not be removed by sublimation, which was a clear indication that this filling was not pore water. In addition, the honeycomb structure in Figure 9 did not deform plastically under the force of gravity, which implied that the structure has yield-strength characteristics. The BSE images showed that the cores of the honeycomb structure are darker when compared to the clayey framework and surrounding clay minerals (Figure 8). This suggested that the cores are filled with a material with relatively low density. Local observations of small open pores on the sample surface indicated the presence of small water-filled pores. The presence of free water in the bentonite sample was confirmed by the breakdown of the vacuum upon heating, which indicates degassing of frozen water.
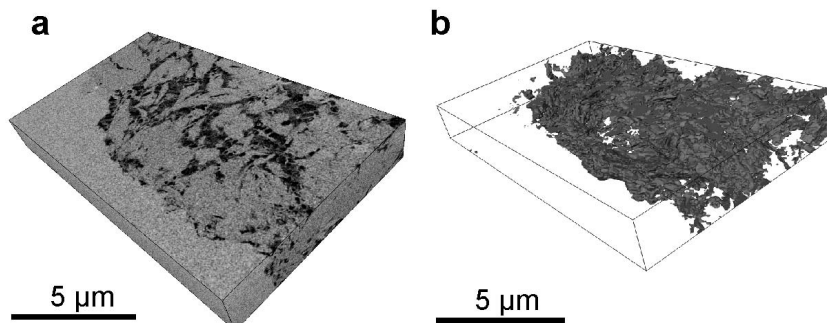

Figure 7. Visualization of FIB-nt data acquired from a bentonite with 1.5 g/cm^3 density (Table 1). (a) Reconstruction of the volume analyzed based on BSE images. (b) 3D reconstruction of the intergranular pore space which is filled with clay gel.
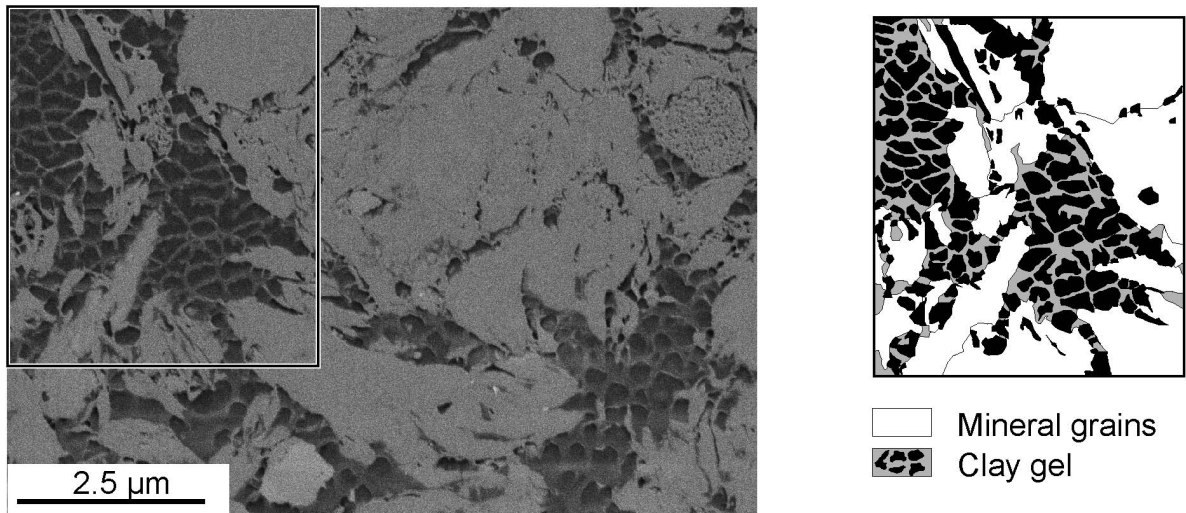
Figure 8. BSE image with marked area corresponding to the sketch (right) showing a domain with abundant large intergranular voids which are filled with a clay gel.

Furthermore, the *in situ* sublimation experiment showed the kinds of microstructural artifacts that can be expected during freeze-drying of the clay samples. The arrows in Figure 9c indicate the cracks which formed during sublimation. Such cracks developed preferentially around larger grains and were probably formed during drying of the fine-grained matrix, which led to

delamination cracks between rigid grains and shrinkage of the clay matrix.

FIB/SEM analysis: density $\approx$ 1.7 g/cm^3

A collection of images and a 3D reconstruction of the pore space, all corresponding to the sample with the highest density, are shown in Figure 10. Note that this
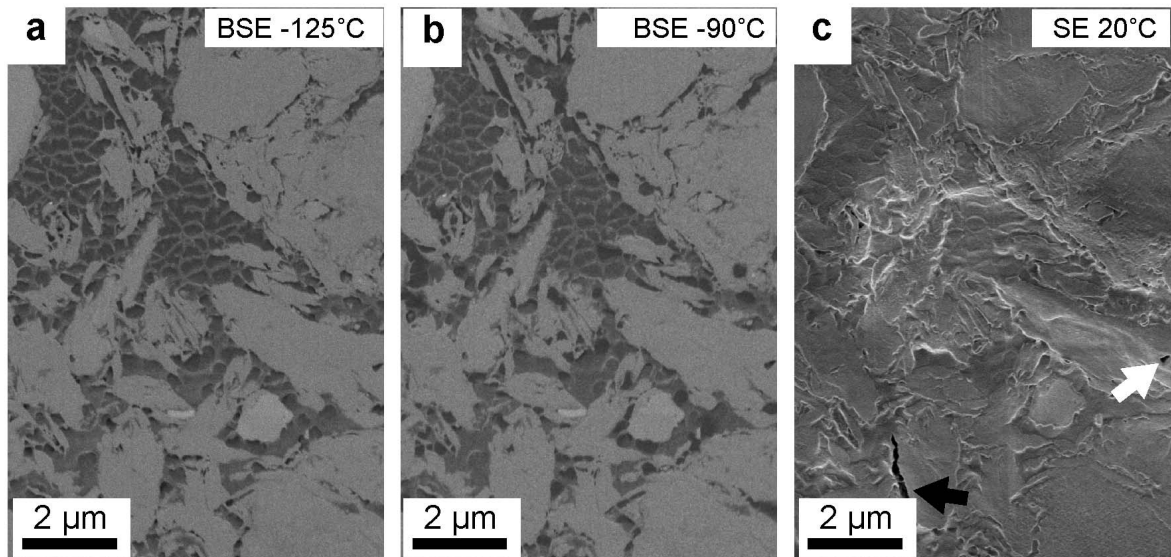

Figure 9. Images showing effects of defreezing, under high vacuum, on the sample with a density of 1.5 g/cm^3, which leads to the sublimation of the amorphous ice in the sample. (a) BSE image showing the material in frozen state (-125ºC). (b) BSE image showing the material at -90ºC and after the start of sublimation. (c) SE image showing the material at room temperatures. The SE image indicates that the majority of the low-density regions observed in the BSE image are filled with a material other than water. The honeycomb structural material does not collapse under the force of gravity, which suggests that the yield strength that may be associated with the low-density filling within the honeycomb cells. Only small numbers of water-filled pores were observed. The white arrow indicates an example of a small empty pore, from which water was removed upon sublimation. The black arrow indicates a crack which formed as a consequence of shrinkage during drying.
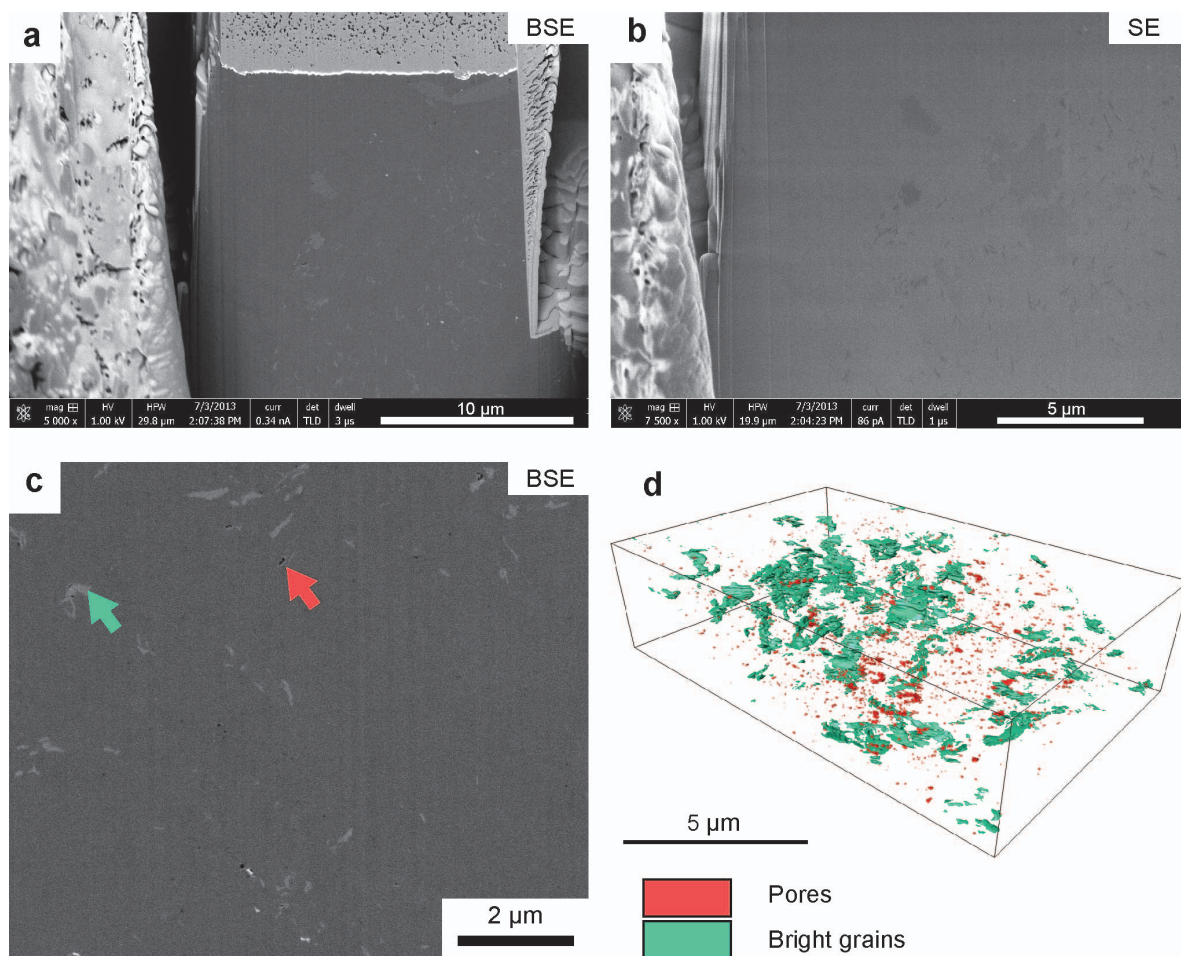
Figure 10. Visualization of the microstructure in bentonite (density of 1.7 g/cm^3) based on data from FIB-nt. (a, b) BSE images of the material analyzed indicating the high density of the material. Clay-gel and larger intergranular pores are absent. (c) A few small intergranular pores can be observed (red arrow). The green arrow indicates a bight mineral present. (d) 3D reconstruction of the pore space (0.1 vol.%) and the bright mineral grains.

sample was more compacted and more water-saturated than the samples at lower densities (Table 1). The microstructure appeared dense (Figure 10a,b,c) and contained numerous bright mineral grains that were dispersed in the clay matrix. These grains are probably impurities (*i.e.* feldspar, calcite). Unlike the low-density samples, clay gel was absent from the sample under consideration. At this higher density, the sample contained only a very small fraction (0.1 vol.%) of open pores. The majority of these rare pores had radii in the 20−30 nm range (Figure 4a). The pore space resolved consisted of isolated pore objects which did not form a connected pore network (Figure 10d).

DISCUSSION

Evolution of intergranular porosity during swelling

Several types of pores have been described in swelling clays. The sizes of pores between mineral layers are in the range of ~1 nm and discontinuities between face-to-face oriented stacks of mineral layers are in the range of 3−4 nm (Tessier, 1990). This pore-size range could not be resolved by FIB-nt. Given the 10 nm resolution (*i.e.* voxel size of FIB-nt), however, the resolved pores with radii >~10 nm were related to the intergranular pore space. Regarding the irregular shape of the clay grains (Figures 2, 3, 8), the resolved pores are obviously linked to geometric incompatibilities between grains or to discontinuities between aggregates of mineral layers, and compaction led to a decrease in the number of these pores and their sizes (Figure 2). The sample material was re-hydrated under unconfined conditions and was subsequently compacted for reasons relating to sample preparation. If re-hydration of compacted dry material occurs under confined (*i.e.* constant volume) conditions, intergranular pore volume accommodates the swelling of the clay minerals. At dry densities of >~1.6 g/cm^3 the initial porosity was interpreted to be too small to accommodate all the swelling, which was supported by a marked increase in swelling

pressure with increasing dry density (Bradbury and Baeyens, 2002). In the present study, reduction in porosity occurred during compaction of re-hydrated material with well defined properties and known dry densities. One might argue that the approach taken led to different microstructures as though swelling occurred under constant-volume conditions. At least in terms of porosity this was obviously not the case because the results obtained were in good agreement with the porosity-reduction process inferred from swelling-pressure curves for materials with different dry densities. The study showed that the intergranular porosity resolved at a dry density of ~1.2 g/cm^3 (water saturation ~70%) is ~5 vol.% and substantially reduced to ~0.1 vol.% if dry densities increase to ~1.7 g/cm^3 (water saturation ~97%). At dry densities of ~1.2 g/cm^3 re-hydrated bentonite still contained air-filled pores, which indicated that most of the water content was in the interlayer region. The breakdown in the vacuum during sublimation inside the SEM sample chamber suggested, however, that some free pore water was present, which was probably stored as external water in pores that were not resolved by FIB-nt.

In terms of the relevance of the approach used to a nuclear-waste repository, where large volumes are to be filled with bentonite backfill material, note that variations in dry densities related to the installation of the backfill could still be observed after 8 years of natural wetting (see Jaremalm *et al.*, 2013). Another cause of density variations was upward swelling which resulted in lower densities in the upper part of the deposition holes. Finally, variations in the water ratio and dry density were observed in different parts of deposition holes (see Jaremalm *et al.*, 2013). Density variations, caused by inhomogeneous swelling and variations in water ratios, suggest that compaction of partially saturated bentonite material requires attention during the safety assessment of bentonite to be used as a backfill material. Hence, the pore microstructure present should be regarded as a potential property of the material to be characterized under application conditions.

For solute transport in dense bentonite, a multi-porosity model with larger intergranular pores and interlayer pores was proposed (*e.g.* Bradbury and Baeyens, 2002). Due to negative surface charging of mineral layers, anions were assumed to be expelled when passing through the interlayer region; water-filled intergranular pores were assumed to represent preferred pathways for anion diffusion. If this is indeed true the connected intergranular porosity (*i.e.* diffusion-accessible porosity) can be estimated on the basis of anion-diffusion experiments. A comparison between the porosity data observed and values calculated for the diffusion-accessible porosity yielded an inconsistent picture. Accounting for the dependence of the accessible porosity on the ionic strength of the pore water, Van Loon *et al.* (2007) calculated the intergranular porosity

on the basis of Cl^- diffusion experiments. At a dry density of 1.2 g/cm^3 an intergranular porosity of ~25 vol.% was calculated which is about five times greater than the measured intergranular porosity in the present study (5.5 vol.%). At a dry density of 1.7 g/cm^3 an intergranular porosity of 8 vol.% was calculated, which is about two orders of magnitude greater than that observed for the same dry density at almost full water saturation (0.1 vol.%). At greater densities in particular, the discrepancy might be related to the fact that FIB-nt only resolved pores with radii $\geqslant 10$ nm and therefore provided no data for smaller pores. Theoretical calculations of the pore sizes in dense bentonite, ignoring the presence of larger pores, suggested that the pore diameter is <10 nm for dry densities >1.2 g/cm^3 and smaller than the interlayer width (*i.e.* three layers of water) for densities >~1.6 g/cm^3 (Tournassat and Appelo, 2011). The present study has documented the presence of a significant proportion of larger pores at lower dry densities, which, in combination with smaller pores, probably form the connected pore network for anion transport. At greater dry densities, larger pores were not present and theoretical calculations showed that the intergranular pore size approaches the value of the width of the interlayer. Regarding the concept of anion exclusion this poses a problem and one must either assume that anions have access to the interlayer regions or the presence of larger pores that are formed as a result of structural modifications at high dry densities. The present study has documented the formation of a clay gel, which is characterized with lower densities (see below) than the surrounding high-density clay grains. Such a bentonite microstructure with an inhomogeneous density distribution could explain anion diffusion at large dry bulk density values.

The nature of 'clay-gel' in bentonite

Regarding the application of bentonite as backfill material, the following scheme of intergranular pore evolution upon water uptake is widely accepted. In the course of water saturation clay aggregates expand and after a sufficiently long time the intergranular pores will be filled by clay gel, which emerges from expanding aggregates. The intergranular pore space is expected to be partly or entirely filled by the clay gel (Liu *et al.*, 2006; Pusch, 2001; Pusch *et al.*, 1990). The formation of clay gels is related to the expansion or swelling of clays. If dry clay is placed in a moist atmosphere, the clay minerals adsorb water vapor in the interlayer region which causes the clay particles to separate or disjoin. This process is referred to as swelling and it proceeds until the separation reaches equilibrium at a given pressure (*e.g.* Luckham and Rossi, 1999). If the concentration of small clay particles is large enough, flocculation will lead to the formation of a continuous gel structure instead of individual flocs (*e.g.* Luckham and Rossi, 1999). The gel structures build up slowly with time, as the particles orient themselves

toward the position of minimum free energy under the influence of the Brownian motion. The concentrations of clay and salt are decisive factors in the length of time required to attain maximum strength (Darley and Gray, 1988). For Na-montmorillonite this concentration is usually >3% (w/w).

The clay content in the material analyzed in the present study was very much greater than that of a typical bentonite suspension which suggests that the 'clay-gel' that is supposed to form in intergranular pores has different properties. This notion is supported by the observation that the thickness of network walls built by face-to-face aggregated sheets depends on the clay concentration (Vali and Bachmann, 1988). Imaging by FIB-nt and SEM revealed that honeycomb-structured clayey material fills the intergranular space between larger clay grains. This material has a mesh-like structure which is similar to the honeycomb structure observed for diagenetic or authigenic smectites. Based on visual comparison, the honeycomb structure observed is better organized when compared to the networks formed in bentonite suspensions (*i.e.* the material is characterized by a better mechanical stability). The volume fraction of clay corresponding to this structure is >~30 vol.% and the thickness of the 'walls' is tens of nanometers. The latter suggest that the walls are built up by more than ten face-to-face mineral layers (Figure 11). Interestingly, the cores or cells of the honeycomb structure are not filled with free water. The BSE images indicate that the core fill has a lower density than the surrounding clayey material leading to the hypothesis that the core fill consists of a clayey material that is structurally different from the surrounding face-to-face aggregates of the honeycomb structure. The lower density might be related to the presence of more water layers between mineral layers (Lagaly and Dékány, 2006) as well as an irregular

organization of mineral layers or stacks of layers, similar to a colloidal gel (Figure 11).

At low dry bulk densities (1.2 g/cm^3), the honeycomb structural material partly fills the intergranular pore space. At intermediate densities (1.5 g/cm^3), this material fills the pores between larger clay grains entirely. At high densities (*i.e.* 1.7 g/cm^3), the clay gel was no longer present. The BSE images of the 1.5 g/cm^3 sample suggested that the clay fraction corresponding to the honeycomb framework is at least 30 vol.%. At such high clay concentrations the paste-like material has yield characteristics and flow resistance under the force of gravity was confirmed *via* 'sublimation' in the SEM.

Saturation occurred under non-confined conditions over an extended period of time and thus it was very likely that the honeycomb-structured material formed during saturation. In such a case, subsequent compaction is expected to modify the delicate structure. This material was only observed at lower dry densities, however, when intergranular pores were still present. The presence of intergranular pores in combination with the evident mechanical strength of the material is probably the reason why the material was largely preserved during compaction after re-hydration. For lower dry densities no reasons were found to exclude the formation of such a honeycomb-structured material in cases where re-hydration occurs under constant volume (*i.e.* under confined conditions). At greater bulk densities (*i.e.* 2.0 g/cm^3) a honeycomb-structured material was not observed and might have been modified beyond recognition during compaction. At such high densities, however, intergranular pores are largely absent and if present the pore radii are on the order of tens of nm. In contrast, the mesh-size corresponding to the clay-gel framework is on the order of 100s of nm long and is thus larger than the pores at high bulk densities. This
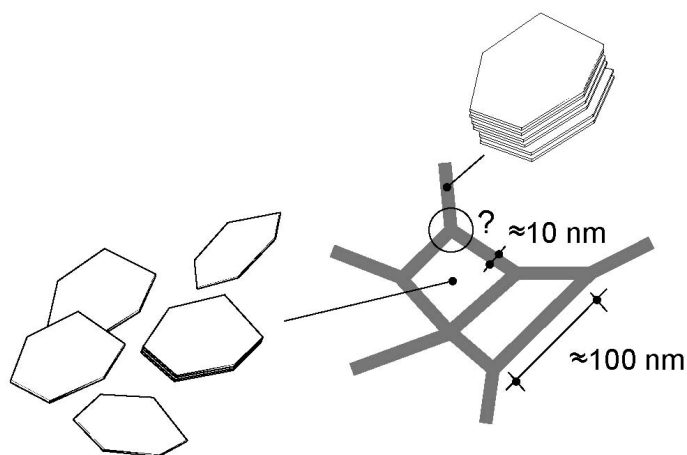

Figure 11. Possible clay-mineral layer associations in the honeycomb-structured material observed. The walls are probably composed of face-to-face-arranged mineral layers. In the cores of the cellular structure, very fine mineral layers are randomly organized and the packing is less dense (similar to colloids with relatively low solid loadings). The low density in the core fillings may also be due to an increased number of water layers between the single mineral layers or between the stacks of mineral layers.

size relation suggests that honeycomb-structured material in intergranular pores can only be formed at comparatively low densities (*i.e.* lower pressures) and in the associated larger intergranular pores. At higher pressures, gelation is obviously suppressed because clay platelets cannot arrange themselves into an energetically stable structure simply due to the lack of space between the larger clay grains.

CONCLUSIONS

A new method was presented, which allowed artifact-free investigation of the microstructures in bentonite samples with different degrees of compaction and associated bulk properties. The method provided systematic results related to MX-80 bentonite microstructures and gave insight into the nature of transport pathways in compacted bentonite.

The generalized picture of an MX-80 bentonite microstructure where a 'clay gel' fills the intergranular pore space can be confirmed. The possibility of deviations from this general picture should be considered, however.

At low densities (*i.e.* dry density of 1.2 g/cm^3) and a water saturation of ~70%, the intergranular pore space was partly filled with a clay gel. At intermediate densities (1.5 g/cm^3), the intergranular pore space was clogged by a clay gel. Further compaction (*i.e.* pressure) apparently suppresses the formation of clay gel because intergranular pores are too small for the formation of the clay framework, which builds the gel. At high densities (1.7 g/cm^3), a percolating network of intergranular pores was not observed.

Microstructural observations suggest that clay gels are preferentially formed in the pressure shadow of larger non-clayey grains. Therefore, the same methods should be applied to a bentonite/sand mixture in order to systematically explore the effects of non-clayey grains on bentonite microstructures.

In addition, the method should be applied more extensively to pure bentonite samples in order to establish crucial relations such as the porosity/density relation, which would shed more light on the systematics of bentonite microstructures for different degrees of compaction and saturation.

ACKNOWLEDGMENTS

REFERENCES

Appelo, C.A.J. (2013) A review of porosity and diffusion in bentonite. *Working report 2013-29*, Posiva, Finland.

Bhuiyan, I. (2013) Microstructural characterization of iron ore green pellets. PhD thesis, Department of Civil, Environmental, and Natural Resources Engineering, Lulea University of Technology, Sweden.

Bourg, I.C., Sposito, G., and Bourg, A.C.M. (2007) Modeling cation diffusion in compacted water-saturated sodium bentonite at low ionic strength. *Environmental Science & Technology*, **41**, 8118−8122.

Bradbury, M.H. and Baeyens, B. (2002) Porewater chemistry in compacted re-saturated MX-80 bentonite − physico-chemical characterization and geochemical modeling. *PSI Bericht 02-10, Paul Scherrer Institut*, Villigen, Switzerland.

Bucher, F. and Müller-Vonmoos, M. (1989) Bentonite as a containment barrier for the disposal of highly radioactive waste. *Applied Clay Science*, **4**, 157−177.

Darley, H.C.H. and Gray, G.R. (1988) *Composition and Properties of Drilling and Completion Fluids*, 5th edition. Gulf Publishing Co., Texas, USA, 643 pp.

Decagon Device Inc. (2002) Dewpoint PotentiaMeter: Operators Manual Version 2.1.

Delage, P. and Cui, Y.J. (2007) Microstructure effects on the hydration and water transport in compacted bentonites used for radiactive waste disposal. Pp. 85−96 in: *Proceedings of 3rd Asian Conference on Unsaturated Soils* (Z. Yin, J. Yuan, and A.C.F. Chiu, editors). Science Press, Beijing, China.

Gens, A. (2010) Mechanics of unsaturated geomaterials applied to nuclear waste storage. Pp. 279−301 in: *Mechanics of Unsaturated Geomaterials* (L. Laloui, editor). John Wiley & Sons, Inc., Hoboken, New Jersey, USA. doi: 10.1002/9781118616871.ch12

Glaus, M.A., Baeyens, B., Bradbury, M.H., Jakob, A., Van Loon, L.R., and Yaroshchuk, A. (2007) Diffusion of ^{22}Na and ^{85}Sr in montmorillonite: Evidence for interlayer diffusion being the dominant pathway at high compaction. *Environmental Science & Technology*, **41**, 478−485.

Glaus, M.A., Birgersson, M., Karnland, O., and Van Loon, L.R. (2013) Seeming steady-state uphill diffusion on ^{22}Na$^+$ in compacted montmorillonite. *Environmental Science & Technology*, **47**, 11522−11527.

Gu, B. and Doner, H.E. (1993) The microstructure of dilute clay and humid acid suspensions revealed by freeze-fracture electron microscopy: reply. *Clays and Clay Minerals*, **41**, 114−116

Herbert, H.J., Kasbohm, J., Moog, H.C., and Henning, K.H. (2004) Long-term behaviour of the Wyoming bentonite MX-80 in high saline solutions. *Applied Clay Science*, **26**, 275−291.

Holzer, L., Münch, B., Rizzi, M., Wepf, R., Marschall, P., and Graule, T. (2010) 3D-microstructure analysis of hydrated bentonite with cryo-stabilized pore water. *Applied Clay Science*, **47**, 330−342.

Jaremalm, M., Köhler, S., and Lidman, F. (2013) Precipitation of barite in the biosphere and its consequences for the mobility of Ra in Forsmark and Simpevarp. SKB report TR-13-28, p. 203, Swedish Nuclear Fuel and Waste Management, Stockholm, Sweden.

Lagaly, G. and Dékány, I. (2006) Colloid clay science. Pp. 243−345 in: *Handbook of Clay Science* (F. Bergaya, B.K.G. Theng, and G. Lagaly, editors). Elsevier, Amsterdam.

Liu, J. and Neretnieks, I. (2006) Physical and chemical stability of the bentonite buffer. SKB report R-06-103, Swedish Nuclear Fuel and Waste Management, Stockholm, Sweden.

Lloret, A. and Villar, M. V. (2007) Advances on the knowledge of the thermo-hydro-mechanical behaviour of heavily compacted "FEBEX" bentonite. *Physics and Chemistry of the Earth*, **32**, 701−715.

Luckham, P.F. and Rossi, S. (1999) The colloidal and rheological properties of bentonite suspensions. *Advances in Colloid and Interface Science*, **82**, 43−92.

Monroy, R., Zdravkovic, L., and Ridley, A. (2010) Evolution of microstructure in compacted London Clay during wetting and loading. *Géotechnique*, **60**, 105−119.

Münch, B. and Holzer, L. (2008) Contradicting geometrical

concepts in pore size analysis attained with electron microscopy and mercury intrusion. *Journal of the American Ceramic Society*, **91**, 4059−4067.

Pusch, R. (2001) The microstructure of MX80 clay with respect to its bulk physical properties under different environmental conditions. Technical Report TR-01-08, Swedish Nuclear Fuel and Waste Management, Stockholm, Sweden.

Pusch, R., Karnland, O., and Hoekmark, H. (1990) GMM − A general microstructural model for qualitative and quantitative studies of smectite calys. Technical Report TR-90-43, Swedish Nuclear Fuel and Waste Management, Stockholm, Sweden.

Saiyouri, N., Hicher, P.Y., and Tessier, D. (2000) Microstructural approach and transfer water modelling in highly compacted unsaturated swelling clays. *Mechanics of Cohesive Frictional Materials*, **5**, 41−60.

Tessier, D. (1990) Behavior and microstructure of clay minerals. Pp. 387−415 in: *Soil Colloids and their Association in Aggregates* (M.F. De Broodt, M.H.B. Hayes, and A. Herbillon, editors). Plenum Press, New York.

Tomioka, S., Kozaki, T., Takamatsu, H., Noda, N., Nisiyama, S., Kozai, N., Suzuki, S., and Sato, S. (2010) Analysis of microstructural images of dry and water-saturated compacted bentonite samples observed with X-ray micro CT.

Applied Clay Science, **47**, 65−71.

Tompkins, R.E. (1981) Scanning electron microscopy of a regular chlorite/smectite (corrensite) from a hydrocarbon reservoir sandstone. *Clays and Clay Minerals*, **29**, 233−235.

Tournassat, C. and Appelo, C.A.J. (2011) Modelling approaches for anion-exclusion in compacted Na-bentonite. *Geochimica et Cosmochimica Act*a, **75**, 3698−3710.

Velbel, M.A. and Barker, W.W. (2008) Pyroxene weathering to smectite: conventional and cryo-field emission scanning electron microscopy, Koua Bocca ultramafic complex, Ivory Coast. *Clays and Clay Minerals*, **56**, 112−127.

Vali, H. and Bachmann, L. (1988) Ultrastructure and flow behavior of colloidal smectite dispersions. *Journal of Colloid and Interface Science*, **126**, 278−291.

Vali, H. and Hesse, R. (1992) The microstructure of dilute clay and humic acid suspensions revealed by freeze-fracture electron microscopy: discussion. *Clays and Clay Minerals*, **40**, 620−623.

Van Loon, L.R., Glaus, M.A., and Mueller, W. (2007) Anion exclusion effects in compacted bentonites: towards a better understanding of anion diffusion. *Applied Geochemistry*, **22**, 2536−2552.